nature communications

Article

https://doi.org/10.1038/s41467-025-59935-4

# Polarization-sensitive in-sensor computing in chiral organic integrated 2D p-n heterostructures for mixed-multimodal image processing

Received: 30 August 2024

Accepted: 6 May 2025

Published online: 19 May 2025

Check for updates

Je-Jun Lee[1,10], Seong-Jun Han[1,2,10], Changsoon Choi[1], Chaewon Seo[3], Seungkwon Hwang[4], Jihyun Kim[5], Jung Pyo Hong[1,2], Jisu Jang[1], Jihoon Kyhm[6], Jung Woo Kim[1,2], Byoung-Soo Yu[1,7], Jung Ah Lim[7,8], Gunuk Wang[2], Joohoon Kang[5], Yonghun Kim[4], Suk-kyun Ahn[3] ✉, Jongtae Ahn[9] ✉ & Do Kyung Hwang[1,2,7] ✉

Sensor-based computing minimizes latency and energy consumption by processing data at the capture point, thereby eliminating extensive data transfer and enabling real-time decision-making. Here, we present a breakthrough in in-sensor computing via circularly polarized light detectors that integrate cholesteric liquid crystal reflectors with two-dimensional van der Waals p-n heterostructures. Our device exhibits a high dissymmetry factor (1.90), allowing effective separation of mixed circularly polarized images, along with a rapid photoresponse (4 μs) and wide linear dynamic range (up to 114.1 dB), suitable for analog multiply-and-accumulate operations in convolution-based in-sensor computing. Harnessing these detectors, we propose mixed-multimodal in-sensor computing using the chiral state of circularly polarized light to dynamically control responsivity, which enables the blending of two arbitrary image processing modes within a single, non-reconfigurable circuit. By effectively integrating polarization-sensitive detectors into the in-sensor computing framework, the proposed architecture preserves kernel optimization capabilities while simplifying circuit complexity.

The majority of imaging tasks today utilize photodiode arrays to transform visual data into electrical signals[1], where the transformation process involves analog-to-digital conversion followed by image processing at the backend. Moving beyond this conventional approach, the advent of in-sensor computing marks a significant shift towards enhancing machine vision capabilities. Processing image data using photodiode arrays as kernels (also known as filters) enables advanced processing capabilities such as real-time edge detection, noise

[1]Center of Quantum Technology, Post-Silicon Semiconductor Institute, Korea Institute of Science and Technology (KIST), Seoul, Republic of Korea. [2]KU-KIST Graduate School of Converging Science and Technology, Korea University, Seoul, Republic of Korea. [3]School of Chemical Engineering, Pusan National University, Busan, Republic of Korea. [4]Energy and Environment Materials Research Division, Korea Institute of materials Science (KIMS), Changwon, Korea. [5]Department of Chemical and Biomolecular Engineering, Yonsei University, Seoul, Republic of Korea. [6]Technology Support Center, Research Resources Division, Korea Institute of Science and Technology (KIST), Seoul, Republic of Korea. [7]Division of Nanoscience & Technology, KIST School, University of Science and Technology (UST), Seoul, Republic of Korea. [8]Soft Hybrid Materials Research Center, Advanced Materials Research Division, Korea Institute of Science and Technology (KIST), Seoul, Republic of Korea. [9]Department of Physics, Changwon National University, Changwon, Republic of Korea. [10]These authors contributed equally: Je-Jun Lee, Seong-Jun Han. ✉e-mail: skahn@pusan.ac.kr; jongtae@changwon.ac.kr; dkhwang@kist.re.kr

reduction, and feature extraction directly at the sensor level[2–4]. Various devices with distinct functionalities have been developed, supporting applications such as pattern recognition, image processing, and visual adaptation, as detailed in Supplementary Table 1.

With ongoing advancements in optoelectronic technologies, circularly polarized light (CPL) stands out for its rich optical information and unique angle-dependent properties[5–7]. These characteristics facilitate a wide range of applications including optical quantum computing[6], bioimaging[8], encryption[9], and three-dimensional (3D) imaging[10]. To date, in-sensor computing incorporating CPL detectors remains unexplored, despite the potential of this approach to offer new possibilities for processing the optical information of CPL. Implementing CPL detectors in such a computing framework demands a high dissymmetry factor as well as rapid and broad linear photoresponses for effective linear vector-matrix multiplication[11,12].

To efficiently manipulate CPL, several types of miniaturized CPL detectors have been developed to replace the multistage process of converting CPL to linearly polarized light using a quarter-wave plate, analyzing it with a polarizer, and finally measuring its intensity using a standard photodetector[13]. The most straightforward strategy employs the unique intrinsic molecular structure of chiral semiconductors for selective polarized light absorption[14]. Despite their critical role in CPL detection, these specialized microstructures face limitations in achieving high charge carrier mobility[15]. One alternative method is to combine circular polarization–sensitive metamaterials with high-mobility semiconductors. Such materials achieve efficient transport by generating carriers that subsequently move to the semiconductors. Modifying the shape, size, and layout of metamaterials through nanoscale photolithography allows for precise tuning of CPL's detectable wavelength range, but this method is complex and expensive[16–18]. A more practical approach integrates cholesteric liquid crystal networks (CLCNs) as chiral optical filters with high-mobility semiconductors; this integration aims to enhance CPL detection performance, including responsivity and dissymmetry factor[9]. The approach uses chiral-selective reflection of CPL from ultraviolet to infrared wavelengths (300–1100 nm), controlled by the pitch of the helix in a CLCN[19]. Despite these advancements, limitations remain in laterally oriented transistor structures, such as inefficient photocarrier separation, resulting in a slow and nonlinear photoresponse due to the photogating effect from trap states at the semiconductor/dielectric interface. Addressing these challenges requires the development of devices that feature a high dissymmetry factor and both rapid and broad linear photoresponses to realize the full potential of polarization-sensitive in-sensor computing.

Here, we present polarization-sensitive in-sensor computing using CPL detectors that combine a chiral organic layer with a two-dimensional (2D) van der Waals (vdW) p-n heterostructure. This integration allows for effective selective detection of CPL through the chiral organic layer and subsequent efficient separation of excited carriers within the 2D vdW heterostructure. The device achieves a high dissymmetry factor (g-factor) of 1.88/ −1.90 for R-form / S-form CLCN-integrated photodiodes (CIPs), respectively. Additionally, by adopting a semi-vertical structure, effective separation of excited carriers in the $MoTe_2/MoS_2$ p-n junction enables a rapid photoresponse, with photocurrent rise/decay times of 4 µs/4 µs along with a broad linear photoresponse across various optical power densities. Owing to its high dissymmetry factor, our device was able to successfully decompose mixed circularly polarized image signals from MNIST and Fashion-MNIST datasets, thereby achieving a high recognition rate in convolutional neural network (CNN) simulations. To explore the potential of our devices for polarization-sensitive in-sensor image processing, we propose polarization-sensitive mixed-multimodal imaging. This technique uses CPL detector arrays within a computational framework to dynamically adjust the blending ratios between any two arbitrary kernels by modulating the polarization states, enabling seamless transitions between image processing modes in a single circuit configuration consisting of only polarization-sensitive non-reconfigurable devices. Dynamic modulation of the responsivity of non-reconfigurable devices using CPL allows one to retain kernel optimization capabilities while significantly reducing circuit complexity. This suggests expanding the degree of freedom of real-time in-sensor image processing by utilizing polarization not merely as a characteristic of light to be observed but as a functional parameter to dynamically control the image processing mode.

## Results

### Device configuration of CLCN-integrated vdW CPL detectors

Figure 1a illustrates the configuration and operational principles of our device. We have developed a CPL detector that incorporates a CLCN film atop a 2D $MoTe_2/MoS_2$ photodiode. The detector identifies CPL via a two-step process: first, it reflects CPL within a specific wavelength range through the CLCN film, and second, it absorbs transmitted light and separates photogenerated carriers with the semi-vertical $MoTe_2/MoS_2$ heterostructure. The $MoTe_2$ and $MoS_2$ serve as p-type and n-type semiconductors, forming a staggered (type II) p-n diode structure. The fabricated CLCN film is dry transferred onto the vdW p-n diode, as confirmed by optical microscopy in Supplementary Fig. 1. To evaluate the CPL-selective properties of our device, we first investigated the transmission of CPL through R-form and S-form configurations of the CLCN film. In the 900–950 nm near-infrared (NIR) region, the R-form CLCN film transmits left-handed circularly polarized light (LH-CPL) while reflecting right-handed circularly polarized light (RH-CPL), whereas the S-form CLCN film exhibited the opposite behavior (Fig. 1b). The dissymmetry factors of the CLCN films were calculated as 1.89 for the R-form and −1.88 for the S-form. The strong chiral optical response was further validated by circular dichroism spectra, which exhibited an ellipticity of approximately 20° at the target wavelength (920 nm) (Supplementary Fig. 2)[20]. Thickness effects of CLCN films were also examined. As the thickness of the R-form CLCN increases, the transmittance for both RH-CPL and LH-CPL decreases. Consequently, the variations in g-factor values remain insignificant (Supplementary Fig. 3). Additionally, the CPL wavelength selectivity can be tuned from the visible to the NIR range by adjusting the helical pitch, which depends on the concentration of the chiral dopant (Supplementary Fig. 4)[19]. Next, we investigated light absorption and carrier separation in a semi-vertical structured vdW p-n photodiode that integrates a Pt bottom electrode directly under the $MoTe_2/MoS_2$ heterostructure (Fig. 1c). This arrangement enhances light absorption and facilitates the collection of photogenerated carriers by minimizing the quasi-neutral area that generates parasitic resistance, thus improving photoresponse speed[21,22]. The band structure of the semi-vertical p-n diode under equilibrium conditions is depicted in Fig. 1d, where the values of the bandgap and sub-bandgap due to intercoupling effects at the heterostructures were confirmed in our previous work[22]. Given that the Fermi level of $MoS_2$ is at a higher energy compared to $MoTe_2$ ($\Delta E_F$ = ~ 0.08 eV), electrons from $MoTe_2$ naturally migrate towards $MoS_2$, creating a built-in potential at their junction[22]. Upon illumination of the heterostructure, photogenerated carriers are efficiently separated by the built-in electric field within the junction area. Strategic placement of the Pt electrode near the vdW heterojunction facilitates the direct collection of these separated carriers, thus enabling a rapid photoresponse. Characterization of our devices was performed using optical microscopy to assess the geometrical configuration, atomic force microscopy to measure thicknesses, and Raman spectrometry to analyze crystallinity (Fig. 1e and Supplementary Fig. 5)[23]. As a control benchmark for integrating the CLCN film, the spectral responsivity of a $MoTe_2/MoS_2$ p-n diode without CLCN film was evaluated in Fig. 1f. The device exhibited a broad detection capability, ranging from the visible to the NIR spectrum (400–1300 nm). This range is nearly compatible

https://doi.org/10.1038/s41467-025-59935-4

with the possible reflection wavelength range of the CLCN film (300–1100 nm)[19]. Upon integrating R-form and S-form CLCN films, a decrease was observed in the responsivity of the R-form CIP towards RH-CPL and of the S-form CIP towards LH-CPL (Fig. 1g). Remarkably, the responsivity profiles of the devices integrated with either R-form or S-form CLCN film for CPL were found to be similar to the responsivity spectrum of the control benchmark sample. This indicates that the integrated CLCN film selectively attenuates the responsivity to specific circular polarizations without significantly affecting the overall detection capabilities of the device across its operational spectrum. We also examined spectral photoresponse measurements of R-form CIPs integrated with CLCN films designed for reflection of 520 nm and 830 nm light, explicitly demonstrating that responsivity in other wavelength ranges can also be selectively attenuated. (Supplementary Fig. 6). Our device concept was validated by mapping spatial photocurrents in the CIPs, as shown in Fig. 1h (R-form) and Fig. 1i (S-form). The variation in spatial photocurrents influenced by CPL chirality demonstrates the effectiveness of the CLCN film, indicating that the p-n junction, particularly in the semi-vertical region where the bottom electrode overlaps, is the predominant site for photocarrier generation.

## Photodiode characteristics of CLCN-integrated photodiodes

Next, considering the spectral photoresponses of the R-form and S-form CIPs, a 904 nm NIR laser diode was chosen as the light source, and the CPL detection characteristics of both forms of CIPs were examined. For the R-form CIP, a significant photovoltaic effect was observed for LH-CPL, where the open-circuit voltage ($V_{OC}$) was 0.24 V and the short-circuit current ($I_{SC}$) was −88.5 nA (Fig. 2a). In contrast, a relatively low photovoltaic effect was observed for RH-CPL in this device, with a $V_{OC}$ and $I_{SC}$ of 0.07 V and −3.4 nA, respectively (Fig. 2b). Conversely, the S-form CIP revealed opposite selectivity, exhibiting weaker photovoltaic effect for LH-CPL with a $V_{OC}$ and $I_{SC}$ of 0.08 V and −4.2 nA, while showing a much more pronounced photovoltaic effect for RH-CPL with a $V_{OC}$ of 0.22 V and $I_{SC}$ of −72.2 nA, respectively (Fig. 2c, d). The difference in photovoltaic properties for CPL is due to the chiral-selective reflection of the R-form and S-form CLCN films. Statistical analysis of several batches of CIPs revealed that $I_{SC}$ exhibited a near-linear relationship with active volume of CIPs (Supplementary Fig. 7). Our device exhibited a nearly ideal (linear) photoresponse to incident optical power density for both R-form and S-form CIPs in photovoltaic mode ($V = 0$ V, without external bias). The linearity parameter ($\alpha$) was extracted from photocurrent variations as a

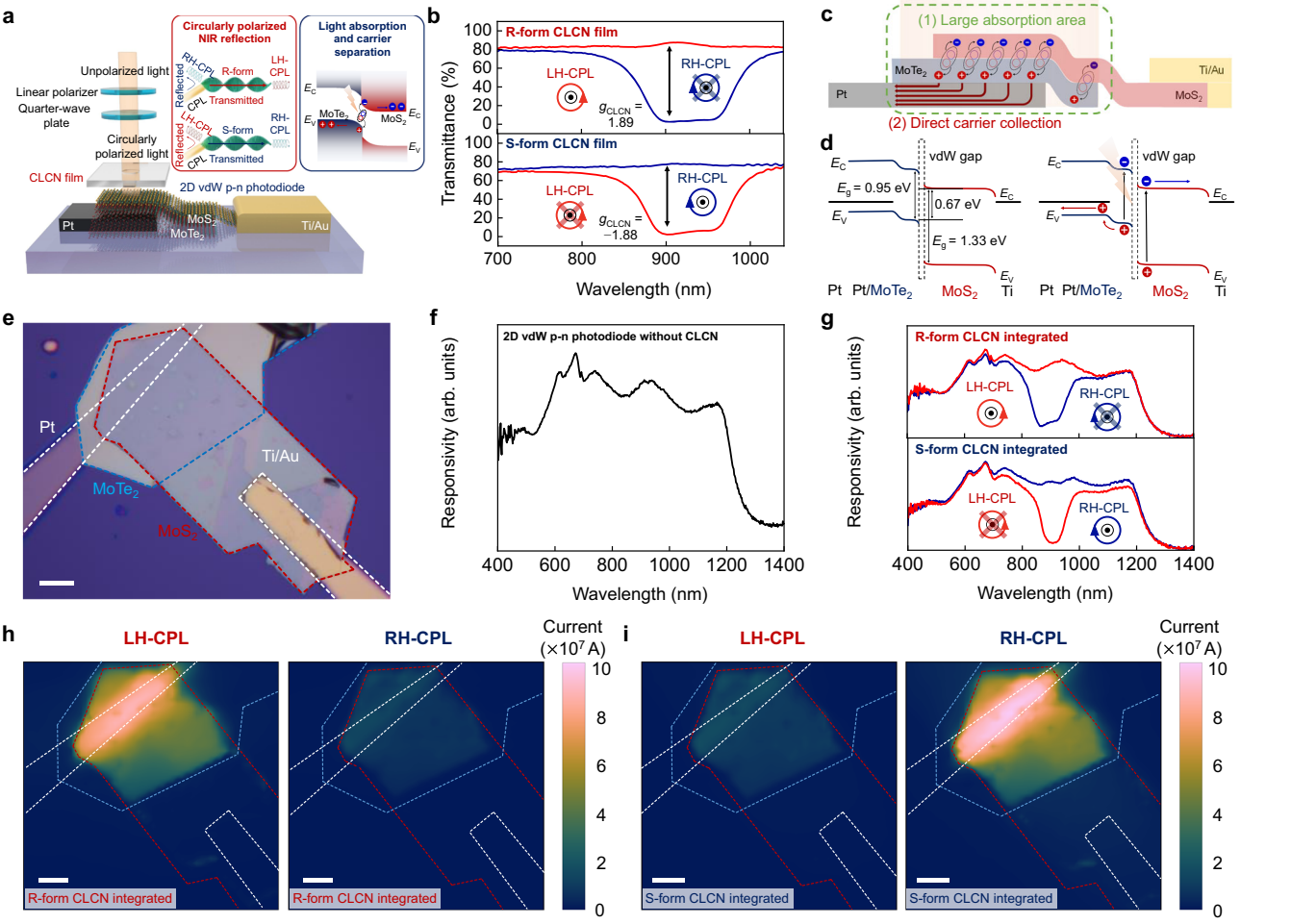


**Fig. 1 | Characterization and performance evaluation of a CPL detector incorporating CLCN film. a** Schematic representation of a circularly polarized light (CPL) detector detailing the operational principle of the device, where selective reflection and absorption of CPL are achieved via cholesteric liquid crystal network (CLCN) film and $MoTe_2/MoS_2$ heterostructure, respectively. **b** Transmission efficiency of CPL through R-form and S-form configurations of the fabricated CLCN film. **c** Schematic representation of a semi-vertical $MoTe_2/MoS_2$ structure, highlighting an effective operational strategy. **d** Band structure of a semi-vertical van der Waals (vdW) $MoTe_2/MoS_2$ p-n diode. **e** Optical microscopy image of a $MoTe_2/MoS_2$ semi-vertical van der Waals p-n diode. Scale bar is 10 μm. **f** Spectral responsivity of a $MoTe_2/MoS_2$ p-n diode without CLCN film, serving as a control benchmark. **g** Responsivity profiles of R-form and S-form CLCN-integrated photodiodes (CIPs). Photocurrent mapping in (**h**), R-form and (**i**), S-form CIPs, respectively. Each panel shows the response under left-handed circularly polarized light (LH-CPL) on the left and right-handed circularly polarized light (RH-CPL) on the right. Scale bar is 10 μm.

https://doi.org/10.1038/s41467-025-59935-4

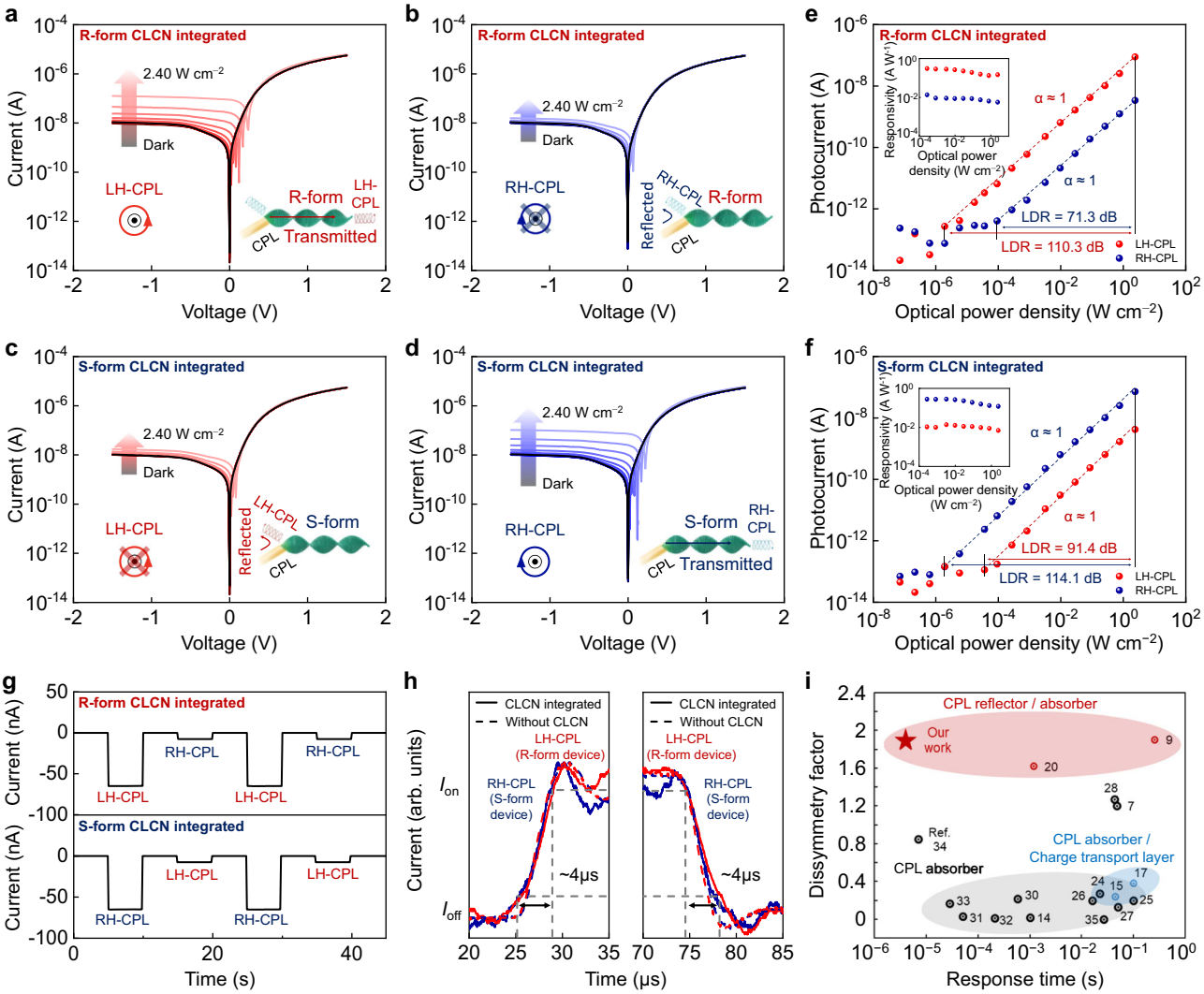


**Fig. 2 | Comprehensive analysis of CPL detection capabilities of CLCN-integrated photodiodes.** *I-V* characteristics when (**a**), LH-CPL and (**b**), RH-CPL are applied to an R-form CIP. *I-V* curve when **c**, RH-CPL and (**d**), LH-CPL are applied to an S-form CIP. Extracted photoresponse with respect to optical power density in photovoltaic mode for the (**e**), R-form CIP and (**f**), S-form CIP. **g** Time-resolved photoresponse of R-form and S-form CIPs to alternating RH-CPL and LH-CPL. **h** Rise and fall times of CIPs for CPL. **i** Benchmarking results of dissymmetry factor and photoresponse time with other CPL detectors.

function of optical power density, as shown in Fig. 2e, f, determined to be approximately 1 for both LH-CPL and RH-CPL. This outcome indicates the absence of complex carrier generation, trapping, and recombination processes within typical semiconductors[21]. The overall equations for extracting the device parameters are given in the Methods section. The linear photoresponse was observed across a wide optical power range. The R-form CIP demonstrated a linear dynamic range of 110.3 dB / 71.3 dB for LH-CPL / RH-CPL, while the S-form CIP correspondingly reached 91.4 dB/114.1 dB. In this range, the responsivity maintained a nearly constant value, as depicted in the insets of Fig. 2e, f, which is particularly advantageous for applications requiring precise detection such as imaging. Almost independent of optical power density in the detectable range, the g-factor values were calculated as 1.88 for the R-form and −1.90 for the S-form CIPs (Supplementary Fig. 8). Notably, the dissymmetry factors of the CIPs are in close agreement with those observed in the CLCN (1.89 for the R-form and −1.88 for the S-form), attributable to the linear photocurrent response of the vdW photodiode to optical power density. The specific detectivity ($D^*$) of R-form and S-form CIPs was estimated to be approximately $10^8$ Jones ($cmHz^{0.5}W^{-1}$), as estimated from the noise power spectral density (refer to Supplementary Fig. 9). External quantum efficiency (EQE) values were also examined, showing 26.7% for LH-CPL in the R-form CIP and 26.31% for RH-CPL in the S-form CIP.

Compared with phototransistors, which show high responsivity as photodetectors owing to their photoconductive gain, photodiodes exhibit significantly faster operation speed. To investigate the dynamic characteristics of our devices, CIPs were exposed to alternating pulses of RH-CPL and LH-CPL (Fig. 2g). In the R-form CIP, photocurrent with LH-CPL was significantly higher than with RH-CPL, while conversely, the S-form CIP displayed much higher photocurrent under RH-CPL compared to LH-CPL, with neither case exhibiting a notable memory effect. The device showed stable operation up to 500 cycles, with a cycle-to-cycle variation of 0.046% (Supplementary Fig. 10). Next, both R-form and S-form CIPs exhibited rapid photocurrent-switching characteristics. Frequency modulation up to 10 kHz resulted in rise and fall times of 4 μs and 4 μs, respectively, for LH-CPL with the R-form CIP and RH-CPL with the S-form CIP. Based on the finding that vdW p-n photodiodes with and without CLCN film exhibited similar photoresponse times, we concluded that CLCN film integration does not compromise the high performance of vdW p-n photodiodes in terms of photoresponse time (Fig. 2h). The devices also exhibited cut-off frequencies exceeding 100 kHz in photovoltaic mode (Supplementary Fig. 11). The performance comparisons

between our CIPs and other CPL detectors in Fig. 2i and Supplementary Table 2 highlight the high dissymmetry factor and rapid photoresponse time of the CIPs. Such results demonstrate the benefits of integrating the highly selective polarization detection capability of CLCN film with the efficient light absorption and carrier separation capabilities of vdW p-n photodiodes[7,9,14,15,17,20,24–35].

### Chiral decomposition and image recognition of mixed circularly polarized images

To evaluate the discrimination capability of the CPL detector, we assess the device's capability to decompose mixed circularly polarized (CP) images containing both LH-CPL and RH-CPL. Decomposition of mixed optical signals components is commonly applied to obtain clear image signals in various fields[5–10]. However, this cannot be achieved through a software-based approach in cases employing achiral photodetectors. When light composed of equal parts LH- and RH-CPL is irradiated onto photodiodes, achiral photodetectors capture both polarizations, leading to images that lose chiral information. In contrast, an R-form CIP filter captures only LH-CPL, while an S-form CIP captures only RH-CPL, allowing a distinct image of each CP component to be obtained, as shown in Fig. 3a (right). In an evaluation of CP imaging for image recognition, the capturing of both chiral signals by achiral photodiodes may lead to misrecognition, for example mistaking the combined signal of "2" and "5" numerals for an "8" as shown in Fig. 3b. In contrast, R-form and S-form CIPs effectively distinguish the specific chiral signals from mixed CPL, enabling accurate recognition of "2" and "5", respectively.

To further confirm this, we prepared a modified MNIST test dataset in which each image is added to the next image to simulate mixed CPL (Mixed CPL in Fig. 3a). Here, we assume that the former image indicates LH-CPL and the latter image indicates RH-CPL. We then emulated image acquisition by R-form and S-form CIPs using the fitted responsivity obtained from Fig. 2e, f, respectively. The images processed from mixed CPL by each device are compared in Supplementary Fig. 12. The recognition rates of these processed images were then evaluated using a CNN trained with the MNIST training dataset using Python with TensorFlow. The architecture of the software-based algorithm consisted of sequential layers aimed at progressively extracting and refining feature maps. We used a stack of convolutional layers with ReLU activations to introduce non-linearity, followed by max-pooling and batch normalization to improve training stability and convergence speed (Fig. 3c top). In detail, a $3 \times 3$ convolutional kernel was applied with 64 filters to detect low-level features, such as edges and corners. This layer was followed by a second $3 \times 3$ convolution layer with 64 filters, also using the ReLU activation function. After each convolutional block, a $2 \times 2$ max-pooling layer down-sampled the feature maps, reducing the spatial dimensions while preserving key information. Subsequent layers increased the filter depth, with two additional convolutional layers, each containing 128 filters and a $3 \times 3$ kernel size, which captured more complex patterns and spatial hierarchies within the images. Another max-pooling and batch normalization layer followed, enhancing the robustness of feature extraction across different training batches. A final convolutional layer with 256 filters applied further refinement, allowing the model to capture high-level abstract features (Fig. 3c bottom). The output from the convolutional blocks was flattened into a one-dimensional vector and passed through a fully connected layer with 512 neurons and a ReLU activation function, enabling the model to learn intricate representations for classification. The final layer consisted of a 10-neuron softmax layer, outputting the probability distribution for each digit class from 0 to 9. We optimized synaptic weights using the Adam optimizer with a learning rate of $10^{-5}$, minimizing the categorical cross-entropy loss over 20 epochs (Fig. 3d). Over 20 training epochs, simulated images processed with both R-form and S-form CIPs achieved a maximum recognition rate of 98.2%, matching the ideal rate obtained with clean MNIST dataset (Fig. 3e). In contrast, the recognition rate for mixed CP images was significantly lower at 45.1%. The discrepancies between predicted numbers and true numbers for each image are depicted using confusion matrices, showing clear enhancement of image recognition capabilities. The confusion matrix for mixed CPL in Fig. 3f revealed significant mispredictions, particularly in misclassifying the value "8". In contrast, as shown in Fig. 3g, h, images captured using photodiodes integrated with both R-form and S-form CIPs demonstrated a marked improvement in accurate recognition. To test the broader applicability of the CIPs, we conducted the same process with a more complex dataset, Fashion-MNIST. Similarly as above, image processing using R-form and S-form CIPs resulted in clearly separated images (Supplementary Fig. 13). In subsequent recognition tests, the processed images achieved recognition rates of 88.0% and 87.8% for the R-form and S-form CIPs, respectively, closely approximating the rate of 88.5% obtained with the clean dataset (Supplementary Fig. 14).

### Zero- and one-dimensional mixed-multimodal image processing

Conventional in-sensor computing relies on an all-reconfigurable-device configuration that maps responsivity values to kernels via the electrostatic doping effect using additional gate terminals[11,36]. Replacing these reconfigurable devices with non-reconfigurable ones with fixed responsivity enables the same (but non-reconfigurable), kernel operation while significantly reducing the extra circuit elements required for responsivity tuning; however, non-reconfigurable kernel operation lacks the optimization capability necessary for more effective image processing. In this context, in-sensor dynamic computing replaces only a subset of the reconfigurable devices with non-reconfigurable ones. Although this approach reduces universality, it still maintains image processing optimization through reconfigurable responsivity tuning, consequently reducing circuit complexity[4]. Inspired by these advancements, we propose a universal approach that enables the dynamic blending of two kernel operations within an all-non-reconfigurable device configuration by continuously adjusting the polarization states of light. Our method retains kernel optimization capabilities while significantly reducing circuit complexity compared to current in-sensor technologies (Supplementary Fig. 15).

To implement polarization-sensitive, in-sensor mixed-multimodal processing with the aid of our CIPs that exhibit a combination of good linearity, high dissymmetry factor, and fast dynamic speed, we examined the photoresponse of CIPs to the continuous modulation of LH-CPL and RH-CPL, a crucial aspect of in-sensor mixed-multimodal image processing. The top panel of Fig. 4a illustrates the generation of various light polarizations, ranging from circular to linear, by adjusting the angle of a half-wave retarder ($\theta$). Here, incident light undergoes polarization through a linear polarizer, after which the polarization direction is modified by rotating a half-wave retarder, causing a $2\theta$ rotation of the polarization direction for every $\theta$ rotation of the retarder. The rotated linearly polarized light, when passing through a subsequent quarter-wave retarder, adopts either linear or circular polarization, contingent upon its angle concerning the optical axis of the quarter-wave retarder. Additional details on this polarization adjustment process involving half-wave and quarter-wave retarders are provided in Supplementary Fig. 16. The bottom panel of Fig. 4a displays the transition of polarized light, representing the change from linear to circular polarization. We next examined the photoresponsivity of both R-form and S-form CIPs depending on the rotated angle of linear polarized light. As depicted in Fig. 4b, despite the non-reconfigurable functionality of the CIPs, the polarized light, varying from linear to circular polarization, induced dynamic changes in photoresponsivity. In the case of CPL, R-form and S-form CIPs exhibited opposite polarimetric responsivities: maximum for left-handed polarization in the R-form CIP and minimum in the S-form CIP, with the

https://doi.org/10.1038/s41467-025-59935-4

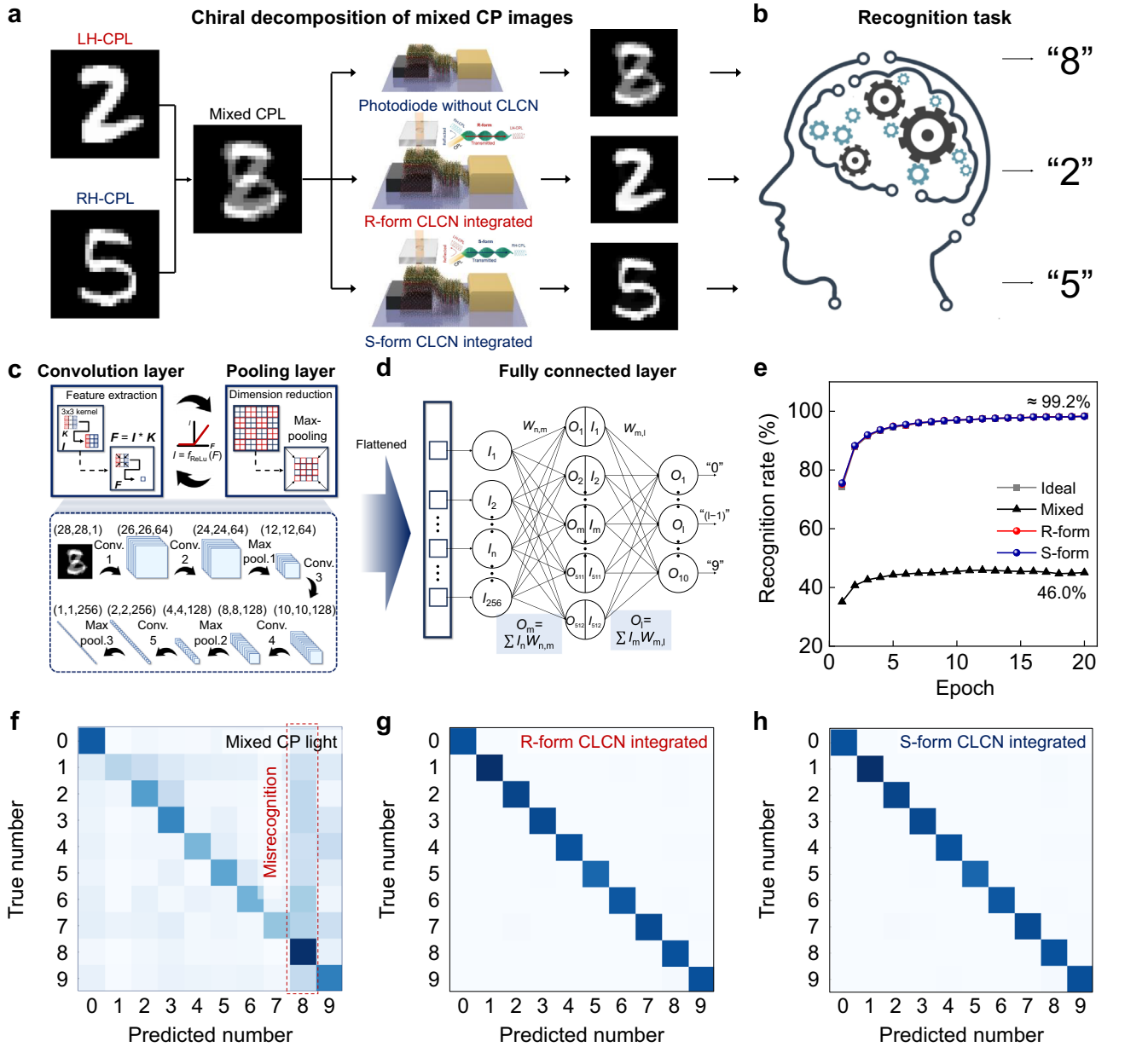


**Fig. 3 | Chiral decomposition and image recognition of mixed circularly polarized images. a** Selective detection of LH-CPL and RH-CPL by R-form and S-form CIPs, enabling distinct image components to be captured. **b** Comparison of image recognition. Conventional photodiodes blur mixed circularly polarized (CP) signals, leading to errors, whereas CIPs accurately distinguish and identify overlapped numerals, enhancing recognition accuracy. **c** Detailed segment of the convolutional neural network (CNN) architecture used for feature extraction, emphasizing convolution, pooling, and rectified linear unit (ReLU) activation functions. **d** Classification process facilitated by the fully connected layer. **e** Comparison of image recognition rates underscoring the superior performance of CIPs for mixed CP images. **f** Confusion matrix for mixed CP images, with subsequent matrices for images processed by (**g**), R-form and (**h**), S-form CIPs demonstrating improved recognition capabilities.

roles reversed for right-handed polarization. For linearly polarized light, the polarization angle was irrelevant to the responsivity due to the inherent rotational symmetry of CLCNs. Moreover, responsivity values for elliptically polarized light, interpolating between linear and circular polarization, showed a distinct sinusoidal dependence on the linear polarization angle ($2\theta$). The time-dependent photocurrent for both R-form and S-form CIPs demonstrated consistent behavior under uniform rotating speed of half-wave retarder (Fig. 4c). This continuous and opposing modulation of responsivity in the chiral opposite CIPs facilitates mixed-multimodal image processing.

As proof of concept, we fabricated a simple zero-dimensional ($1 \times 1$) polarimetric array of CIPs with a kernel value of +1 (identity) for the R-form CIP and −1 (negation) for the S-form CIP (Fig. 4d). In this configuration, two devices connected in parallel simultaneously generate photocurrents in opposite directions in photovoltaic mode ($V = 0$ V), which are summed according to Kirchhoff's law. This accumulated current is then converted to voltage using a transimpedance amplifier (TIA) for practical use[11]. An optical microscopic image of zero-dimensional polarimetric array is presented in Supplementary Fig. 17. Each device selectively absorbs light of different polarization, resulting in a positive photocurrent under LH-CPL illumination and a negative photocurrent under RH-CPL illumination (Fig. 4e). Figure 4f shows the output voltage ($V_{out}$) of the $1 \times 1$ polarimetric array, where the polarization state varies by rotating the half-wave retarder. As the polarization state changes, $V_{out}$ dynamically varies from negative to positive without the need for an additional responsivity control terminal.

https://doi.org/10.1038/s41467-025-59935-4

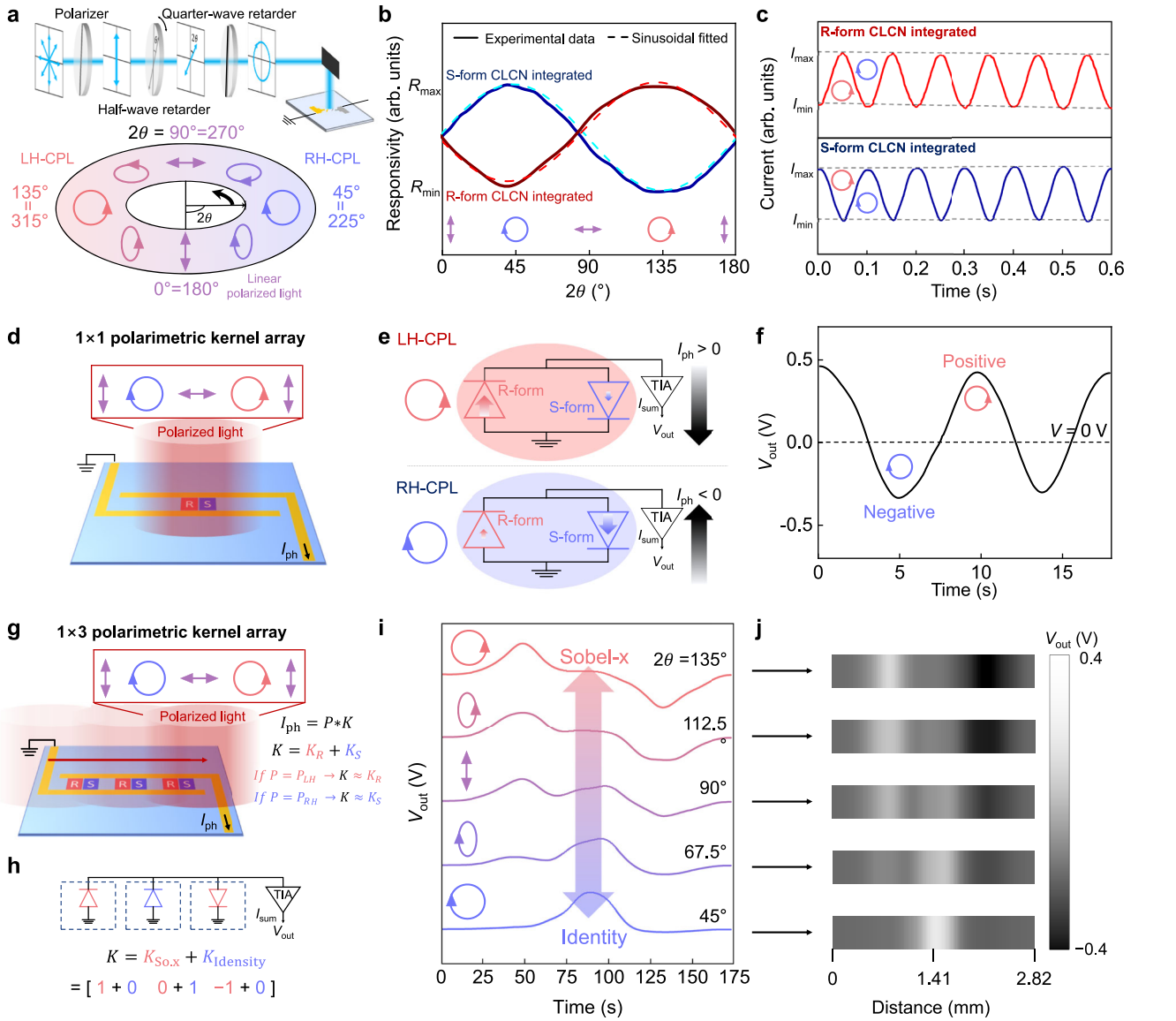


**Fig. 4 | Zero- and one-dimensional mixed-multimodal image processing. a** (Top) Illustration of polarized light generation methods transitioning from circular to linear polarization. (Bottom) Display of polarized light variations achieved through the adjustment of the angle of a half-wave retarder. **b** Responsivity of R-form and S-form CIPs to linear and circularly polarized light. **c** Time-resolved photocurrent measurements to characterize R-form and S-form CIP behavior with a half-wave retarder rotating six times at a uniform speed. **d** Schematic of a 1 × 1 polarimetric array with integrated localized CLCN on vdW photodiodes. **e** Photocurrent behavior of the 1×1 array under LH-CPL and RH-CPL illumination. **f** $V_{out}$ of the 1 × 1 array as the polarization state varies. **g** Schematic of a 1 × 3 polarimetric array illustrating analog convolution of incident light and CIP responsivities. **h** Circuit illustration polarimetric kernel consisting of Sobel-X (R-form) and identity (S-form). **i** Measured voltage signal over time during a 904 nm spot scan across the array under different polarizations. **j** Spatially processed voltage signals by polarimetric kernel array.

Next, we fabricated a one-dimensional (1 × 3) polarimetric array of CIPs to demonstrate the polarization-sensitive, in-sensor mixed multimodal imaging process for a cross section of light. In this configuration, as a light spot traverses the entire 1 × 3 photodiode array from left to right, analog convolution between the 1 × 3 incident polarized light power ($P$) and the programmed 1 × 3 responsivity ($K$) for each CIP produces individual currents that sum according to Kirchhoff's current law. (Fig. 4g). Here, the parameter $K$ can dynamically vary from $K_R$ to $K_S$, depending on the applied polarized state of light and the degree of superposition between LH-CPL and RH-CPL. The polarimetric kernel is designed as a Sobel-X filter using R-form CIPs and as an identity filter using S-form CIPs, while the TIA converts the accumulated currents into $V_{out}$ (Fig. 4h). For the application, we implemented localized CLCN directly integrated on vdW photodiodes (Supplementary Fig. 18). The fabrication process of localized CIPs is shown in Supplementary Fig. 19. The transmittance of the CLCN fabricated using this method, along with the photoresponse of the directly integrated CIPs, confirmed sufficient circular polarization detection capability up to microscale size (Supplementary Figs. 20 and 21). Figure 4i illustrates the measured $V_{out}$ over time as 904 nm light is scanned from left to right across the polarimetric kernel array. Under LH-CPL illumination, both positive and negative voltage responses are observed when the edge of the light spot crosses the kernel. In contrast, under RH-CPL illumination, only positive voltage response is observed as the center of the light spot traverses the kernel. By adjusting the half-wave retarder angle ($2\theta$), a mixed polarization state is generated, resulting in a superposition of the two voltage responses. Given the measured light velocity of 16.21 μm $s^{-1}$, these results can be interpreted in terms of one-dimensional spatial imaging for cross-section of incident light (Fig. 4j). The processing function transitions from an identity operation to Sobel-X filtering based on the polarization

https://doi.org/10.1038/s41467-025-59935-4

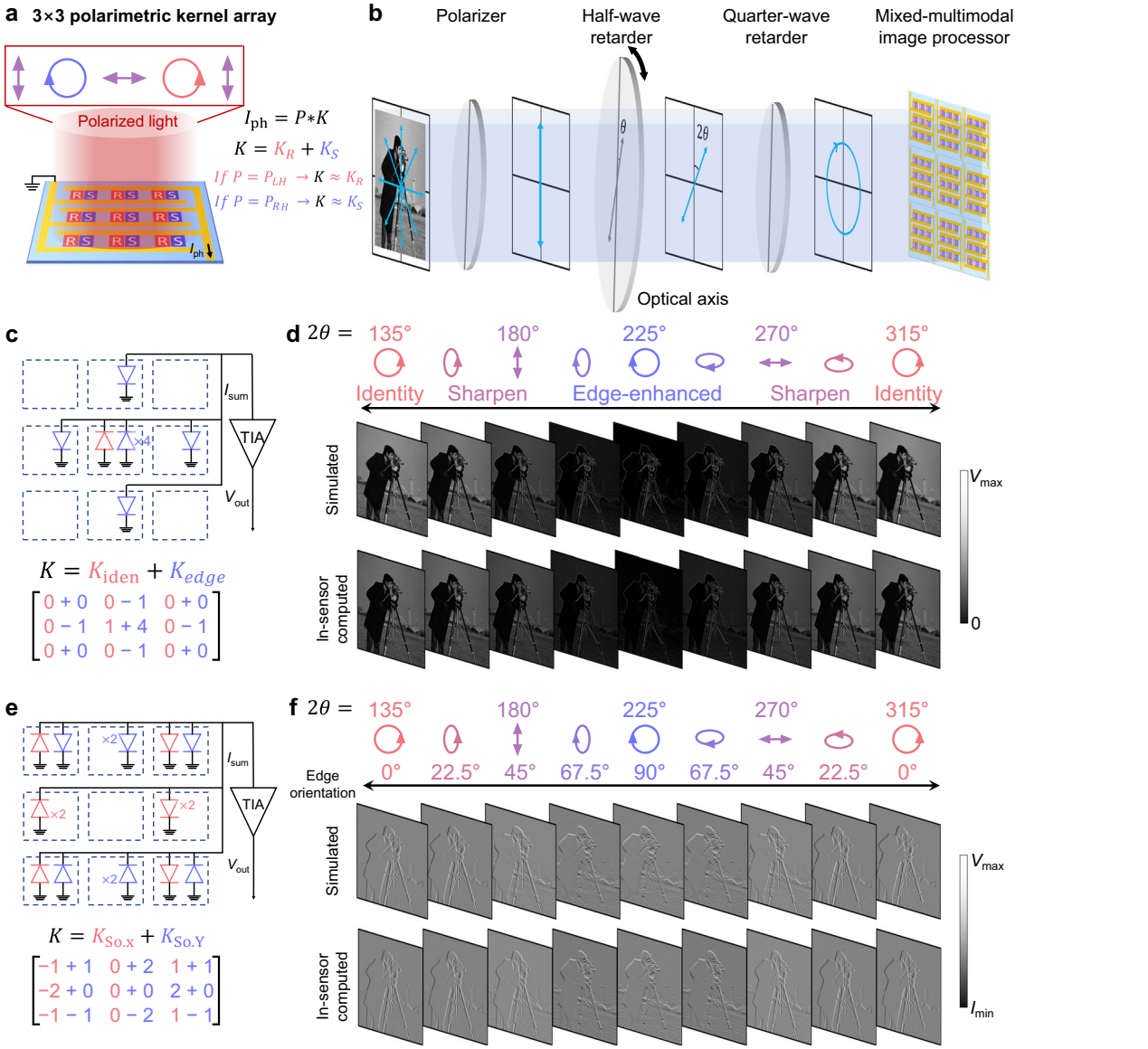


**Fig. 5 | Two-dimensional polarization-sensitive mixed-multimodal imaging.** **a** Layout of a 3 × 3 polarimetric kernel array designed for polarization-sensitive image processing, enabling distinct detection and processing of images based on polarization chirality. **b** System depiction of continuous polarized image generation and subsequent processing via a 3 × 3 polarimetric kernel array, illustrating the concept of polarization-sensitive in-sensor mixed-multimodal imaging. **c** Circuit illustration for polarimetric kernels consisting of identity and edge-enhancement operation. **d** Comparison of simulated results (assuming an ideal dissymmetry factor of 2) and in-sensor computed emulation, showing the seamless transition from identity filtering to edge-enhanced imaging with varying polarization angles using the Cameraman image. **e** Circuit illustration for polarimetric kernels consisting of identity and edge-enhancement. **f** Transition of processed image from Sobel-X to Sobel-Y processed images with changing polarization angles, enabling angle-dependent edge detection. The Cameraman image is adapted from (© Massachusetts Institute of Technology, used under the CC BY-NC 4.0 license).

state, successfully demonstrating polarization-sensitive, in-sensor mixed multimodal computing.

## Two-dimensional polarization-sensitive mixed-multimodal imaging

Based on the above result, we conceptually constructed a 3 × 3 polarimetric kernel array for a polarization-dependent, mixed-multimodal image processor to demonstrate the potential of our device for mixed-multimodal imaging. (Fig. 5a). The kernel array consists of CPL photodiodes connected in parallel for convolution operation, where the responsivity values corresponding to the kernel matrix are determined by their number and positions. By adjusting the polarization state, the programmed kernel values can be continuously tuned, spanning kernels matrix configured from R-form CIPs to those with S-form CIPs. Here, the analog convolution between the 3 × 3 incident polarized light power ($P$) and the programmed 3 × 3 responsivity ($K$) for each CIP produces individual currents that sum according to Kirchhoff's current law. The parameter $K$ can dynamically vary from $K_R$ to $K_S$, depending on the applied polarized state of light and the degree of superposition between LH-CPL and RH-CPL. A system for generating continuous polarized images and subsequent processing by a mixed-multimodal image processor, consisting of a 3 × 3 polarimetric kernel array, is shown in Fig. 5b, where the generation of a polarized image follows the explanation in Fig. 4a. The image utilized here illustrates common intensity information, and our system performs mixed-multimodal processing by polarizing this intensity information and subsequently processing it using polarization-sensitive kernels.

To test the versatility of this concept we investigated three distinct mixed-multimodal imaging techniques: identity with edge-enhanced features, Sobel-X and Sobel-Y, and a combination of blurring and sharpening. In each case, we combined kernel arrays with R-form and S-form photodetectors to generate mixed kernels. The circuit diagram in Fig. 5c depicts the generation of an output signal from a mixed kernel, integrating identity and edge enhancement, through the summation of currents from two distinct $3 \times 3$ polarization-sensitive photodetector arrays[4]. We note that $V_{out}$ is set to zero if $V_{out}$ is less than zero[4]. We compared the simulated result (which assumes an ideal dissymmetry factor of 2) with an in-sensor computed one using a widely utilized stock photo known as the Cameraman image. Here, the mixed-multimodal image processor used the fitted responsivity obtained from Fig. 2e, f. Applying polarization states that vary with the polarization angle ($2\theta$), seamless transitions of the processed image from identity filtering to edge-enhanced imaging were achieved, as shown in Fig. 5d and Supplementary Video 1. Identity filtering preserves the static features of an image, while edge enhancement accentuates boundaries and transitions to highlight dynamic features. By continuously blending these two techniques—from identity to edge detection—through polarization modulation, we anticipate high applicability in fields requiring the analysis of both static and dynamic elements, like autonomous driving[4]. Compared to the simulated result, the in-sensor computed result exhibits partial mixing between the two kernels even under conditions of unmixed polarization, which is due to the incomplete suppression of photocurrent generation from untargeted CPL devices. Nonetheless, the high dissymmetry factor of the CPL device does not critically compromise the result. Figure 5e presents another mixed-multimodal image processing method that uses a circuit diagram to process Sobel-X and Sobel-Y kernel combinations. The distinction between this method and that in Fig. 5c lies in the configuration of the photodetectors along different kernel matrices. As the angle of the polarized light to the quarter-wave plate shifts from 135° to 225°, the processed image exhibits a seamless transition from Sobel-X to Sobel-Y processing, enabling angle-dependent edge detection from 0° to 90° (Fig. 5f). The third application, i.e., blurring and sharpening, is explored in Supplementary Fig. 22. Specifically, the blurring kernel effectively reduces noise but diminishes image contrast, whereas the sharpening kernel enhances contrast yet can amplify noise. By optimally mixing these two kernels, the method achieves a targeted compromise between noise reduction and contrast enhancement. Following confirmation of the universality of mixed-multimodal image processing, the potential to dynamically optimize the mixed-kernel techniques can be explored. Although our work validated potential of polarimetric $3 \times 3$ kernel operation through emulation, a realistic implementation of a large-scale $3 \times 3$ array-level mixed multimodal computing system can be achieved through two key advancements: (i) the development of p-n diodes based on uniformly grown large-area vdW films and (ii) equipment capable of precisely depositing CLCN liquid in defined quantities and positions[37]. Template-assisted processing of the CLCN liquid, combined with capillary-driven injection can be employed for the micro-patterning of CLCN[38]. We are currently in the preparatory stage of implementing a $3 \times 3$ array using large-area vdW films (Supplementary Fig. 23). By integrating precise localized-CLCN printing technology with fabricated large-area vdW p-n films, we anticipate that a large-area polarimetric kernel array composed of low-variation CIP elements can be realized.

## Discussion

Our research presents an approach in the field of in-sensor computing that adopts CPL detectors combining chiral organic layers with 2D van der Waals p-n heterostructures. This design enables the selective detection of CPL and the efficient separation of charge carriers, as evidenced by significant dissymmetry factors and fast photoresponse times. Our device successfully discriminated mixed CP image signals, achieving a high recognition rate at CNN simulation. This capability is particularly valuable for recognizing chiral-selective circularly polarized image signals in fields such as biomolecular and environmental analysis. Building on this advancement, we proposed an approach that integrates polarization-sensitive non-reconfigurable photodetectors, enabling dynamic blending of two arbitrary kernel operations, through polarization state adjustments. This method retains optimization capabilities while significantly reducing circuit complexity. Our results underscore the utility of polarization-dependent manipulation in introducing additional degree of freedom to image processing and analysis, potentially transforming research and applications across various fields by improving machine vision capabilities.

## Methods

### Preparation of directly stackable free-standing CLCN films

Glass substrates were first cleaned using acetone and isopropyl alcohol followed by $O_2$ plasma treatment for 10 min to enhance surface adhesion. The prepared substrates were then coated with a poly(amic acid) solution (SE6514, Nissan) using a spin-coating technique. Subsequent prebaking at 70 °C for 5 min aimed to evaporate solvent residues, followed by thermal imidization at 200 °C for 60 min to achieve the final polyimide layer. The surface of the coated polyimide was mechanically aligned by rubbing with a velvet cloth to ensure uniform orientation. To construct the cell, rubbed glass substrates were positioned in an antiparallel configuration, creating a planar alignment condition. The cell gap was regulated by integrating glass rod spacers with an optical adhesive. To prepare planar aligned CLCN films, a mixture of nematic monomer (RM82, 93.1 wt%), chiral dopant (R-1011 or S-1011, 5.1 wt%), and photoinitiator (Irgacure-651, 1.8 wt%) was prepared in a 5 mL vial. After thorough mixing using a vortex under heat, the homogeneous cholesteric liquid crystal mixture was introduced into a planar cell via capillary action. Photopolymerization was then performed using UV light ($\lambda = 365$ nm) to solidify the mixture. Finally, the resulting free-standing CLCN films, approximately 32 µm thick, were removed from the cell.

### Device fabrication

The 2D $MoTe_2/MoS_2$ heterojunction photodiodes were fabricated on $SiO_2$ (285 nm)/Si substrates. Commercial 2D single crystals of $MoTe_2$ and $MoS_2$ were prepared through mechanical exfoliation and transferred onto the substrate using a polydimethylsiloxane (PDMS) stamp. Ti/Pt (5/10 nm) and Ti (10 nm)/Au (40 nm) served as the bottom and top electrodes, respectively, patterned using conventional photolithography. Next, the prepared CLCN film was dry transferred onto the p-n diode.

### Material and device characterization

The thicknesses of the $MoTe_2$ and $MoS_2$ nanoflakes were measured using atomic force microscopy with a Park Systems NX10. Raman spectroscopy (LabRAM HR Evolution, Horiba Jovin-Yvon) with a laser excitation wavelength of 532 nm was used to characterize the crystallinities and qualities of $MoTe_2$ and $MoS_2$. Microfocused absorption measurements were carried out to analyze the material properties. Based on this measurement, the circular dichroism spectra of the CLCN film were calculated by multiplying the absorbance difference between RH-CPL and LH-CPL by a conversion factor of 32.98°[39]. Static behaviors of the photodiodes, both in the dark and under various light illuminations, were characterized using semiconductor parameter analyzers (Keithley 2636B and Agilent 4156 C). To calculate the parameter $D^*$, we measured the noise power spectral densities using an SR 570 low-noise-current preamplifier and an Advantest R9211B digital spectrum analyzer. Light sources included near-infrared (NIR) laser diodes (904 nm L904P010 and 808 nm L808P200) from Thorlabs, Inc. For the measurement of CP-dependent characteristics, a linear

polarizer (Thorlabs, LPVIS050), a half-wave retarder (Newport, 10RP52 − 2), and a quarter-wave retarder (Thorlabs, SAQWP05M-700) were utilized. Details on the setups for measuring dynamic properties, including photoelectrical bandwidth, were made with a high-speed oscilloscope (Tektronix TDS2024) coupled with a function generator (Tektronix AFG31000). Photocurrent mapping was conducted using a scanning photocurrent system (Nanobase), where the laser beam was transmitted to the confocal microscope through optical lenses and fibers. An ultra-long working distance (ULWD) ×100 objective lens was used to achieve a sub-1 to 100 μm beam spot. The spatial photocurrent distribution was mapped by scanning the focused laser beam across the stationary sample using a galvanometer-based x–y beam scanner. A motorized x–y stage was used for sample positioning before measurement. Photocurrent signals were measured using a Keithley 2636B source meter. All measurements were conducted inside a dark-shielded box (MSTECH) to minimize external interference. In the same manner, a working distance ×10 objective lens was used to achieve few-mm beam spot to measure 1 × 1 and 1 × 3 polarimetric kernel array, respectively.

### Equations for extracting optoelectronic parameters

The linearity parameter ($\alpha$) is determined by the equation $I_{ph} = BP^{\alpha}$, where $I_{ph}$ is the photocurrent, $B$ is a constant, $P$ is the optical power density, and $\alpha$ is a fitted linearity parameter. The linear dynamic range is defined as $LDR = 20\log I_{ph}/I_{dark}$, where $I_{ph}$ and $I_{dark}$ are the photocurrent and dark current, respectively, and the dissymmetry factor (g-factor) is calculated using the formula $g_{CLCN} = \frac{2(I_{LH}-I_{RH})}{I_{LH}+I_{RH}}$ and $g_{detector} = \frac{2(I_{LH}-I_{RH})}{I_{LH}+I_{RH}}$, where $I_{LH}$ and $I_{RH}$ are the photocurrent under LH-CPL and RH-CPL, respectively.

The specific detectivity ($D^*$) of the devices is evaluated using $D^* = \frac{R\sqrt{A}}{S_n}$, where $R$ is the responsivity, $A$ is the device area, and $S_n$ is the noise power spectral density. The analysis incorporates three types of $S_n$ values: experimental noise, and theoretical values for thermal noise and shot noise. The thermal noise is calculated as $S_{n,thermal} = \sqrt{\frac{4kT\Delta f}{R}}$ and the shot noise as $S_{n,shot} = \sqrt{2qI\Delta f}$, where $k$ is the Boltzmann constant, $T$ is the temperature, $R$ is the resistance at near-zero bias, $q$ is the elementary charge, $I$ is the dark current, and $\Delta f$ is the bandwidth. Details of these comparisons are discussed in both the main text and the Supplementary Information.

## Data availability

All figure data generated in this study are provided in the Source Data file. Source data are provided with this paper.

## Code availability

Any codes used in this study are available online in a "Code Ocean" [https://doi.org/10.24433/CO.0197564.v1].

## References


1. Park, J. et al. 7.9 1/2.74-inch 32Mpixel-prototype CMOS image sensor with 0.64 μm unit pixels separated by full-depth deep-trench isolation. *In 2021 IEEE International Solid-State Circuits Conference (ISSCC)* Vol. 64, 122–124 (IEEE, 2021).
2. Chai, Y. In-sensor computing for machine vision. *Nature* **579**, 32–33 (2020).
3. Zhou, F. & Chai, Y. Near-sensor and in-sensor computing. *Nat. Electron.* **3**, 664–671 (2020).
4. Yang, Y. et al. In-sensor dynamic computing for intelligent machine vision. *Nat. Electron.* **7**, 225–233 (2024).
5. Lodahl, P. et al. Chiral quantum optics. *Nature* **541**, 473–480 (2017).
6. Sherson, J. F. et al. Quantum teleportation between light and matter. *Nature* **443**, 557–560 (2006).
7. Song, I. et al. Helical polymers for dissymmetric circularly polarized light imaging. *Nature* **617**, 92–99 (2023).
8. Heffern, M. C., Matosziuk, L. M. & Meade, T. J. Lanthanide probes for bioresponsive imaging. *Chem. Rev.* **114**, 4496–4539 (2014).
9. Han, H. et al. High-performance circularly polarized light-sensing near-infrared organic phototransistors for optoelectronic cryptographic primitives. *Adv. Funct. Mater.* **30**, 2006236 (2020).
10. Zhang, M. et al. Processable circularly polarized luminescence material enables flexible stereoscopic 3D imaging. *Sci. Adv.* **9**, eadi9944 (2023).
11. Jang, H. et al. In-sensor optoelectronic computing using electrostatically doped silicon. *Nat. Electron.* **5**, 519–525 (2022).
12. Yu, S., Jiang, H., Huang, S., Peng, X. & Lu, A. Compute-in-memory chips for deep learning: recent trends and prospects. *IEEE Circuits Syst. Mag.* **21**, 31–56 (2021).
13. Zhang, C., Wang, X. & Qiu, L. Circularly polarized photodetectors based on chiral materials: a review. *Front. Chem.* **9**, 711488 (2021).
14. Chen, C. et al. Circularly polarized light detection using chiral hybrid perovskite. *Nat. Commun.* **10**, 1927 (2019).
15. Zhu, D. et al. Organic donor-acceptor heterojunctions for high performance circularly polarized light detection. *Nat. Commun.* **13**, 3454 (2022).
16. Li, W. et al. Circularly polarized light detection with hot electrons in chiral plasmonic metamaterials. *Nat. Commun.* **6**, 8379 (2015).
17. Jiang, Q. et al. Ultrathin circular polarimeter based on chiral plasmonic metasurface and monolayer $MoSe_2$. *Nanoscale* **12**, 5906–5913 (2020).
18. Chang, Y.-C. et al. High-throughput nanofabrication of infra-red and chiral metamaterials using nanospherical-lens lithography. *Sci. Rep.* **3**, 3339 (2013).
19. Xiang, J. et al. Electrically tunable selective reflection of light from ultraviolet to visible and infrared by heliconical cholesterics. *Adv. Mater.* **27**, 3014–3018 (2015).
20. Wang, Q. et al. High-performance organic narrow dual-band circular polarized light detection for encrypted communications and color imaging. *Adv. Mater.* **36**, 2312396 (2024).
21. Lee, H. et al. 2D $WSe_2/MoS_2$ van der Waals heterojunction photodiode for visible-near infrared broadband detection. *Appl. Phys. Lett.* **113**, 163102 (2018).
22. Ahn, J. et al. Self-powered visible–invisible multiband detection and imaging achieved using high-performance 2D $MoTe_2/MoS_2$ semi-vertical heterojunction photodiodes. *ACS Appl. Mater. Interfaces* **12**, 10858–10866 (2020).
23. Ferrari, A. C. & Basko, D. M. Raman spectroscopy as a versatile tool for studying the properties of graphene. *Nat. Nanotechnol.* **8**, 235–246 (2013).
24. Wang, J. et al. Aqueous synthesis of low-dimensional lead halide perovskites for room-temperature circularly polarized light emission and detection. *ACS Nano* **13**, 9473–9481 (2019).
25. Ma, J. et al. Chiral 2D perovskites with a high degree of circularly polarized photoluminescence. *ACS Nano* **13**, 3659–3665 (2019).
26. Wang, L. et al. A chiral reduced-dimension perovskite for an efficient flexible circularly polarized light photodetector. *Angew. Chem. Int. Ed.* **59**, 6442–6450 (2020).
27. Shang, X. et al. Surface-doped quasi-2D chiral organic single crystals for chiroptical sensing. *ACS Nano* **14**, 14146–14156 (2020).
28. Shi, W. et al. Fullerene desymmetrization as a means to achieve single-enantiomer electron acceptors with maximized chiroptical responsiveness. *Adv. Mater.* **33**, 2004115 (2021).
29. Zhang, X. et al. Great amplification of circular polarization sensitivity via heterostructure engineering of a chiral two-dimensional hybrid perovskite crystal with a three-dimensional $MAPbI_3$ crystal. *ACS Cent. Sci.* **7**, 1261–1268 (2021).
30. Li, D. et al. Chiral lead-free hybrid perovskites for self-powered circularly polarized light detection. *Angew. Chem. Int. Ed.* **60**, 8415–8418 (2021).

31. Liu, L. et al. Chiral non-fullerene acceptor enriched bulk heterojunctions enable high-performance near-infrared circularly polarized light detection. *Small* **18**, 2202941 (2022).
32. Liu, L., Wei, Z. & Meskers, S. C. J. Semi-transparent, chiral organic photodiodes with incident direction-dependent selectivity for circularly polarized light. *Adv. Mater.* **35**, 2209730 (2023).
33. Liu, L. et al. Building supramolecular chirality in bulk heterojunctions enables amplified dissymmetry current for high-performing circularly polarized light detection. *ACS Mater. Lett.* **4**, 401–409 (2022).
34. Ward, M. D. et al. Highly selective high-speed circularly polarized photodiodes based on π-conjugated polymers. *Adv. Opt. Mater.* **10**, 2101044 (2021).
35. Gu, Q. et al. Constructing chiral covalent-organic frameworks for circularly polarized light detection. *Adv. Mater.* **36**, 2306414 (2023).
36. Mennel, L. et al. Ultrafast machine vision with 2D material neural network image sensors. *Nature* **579**, 62 (2020).
37. Lee, H. et al. Transferred Chiroptical Transitions in Chiral Binaphthyl /π-Conjugated Polymer Hybrid Films: Significance of Aromatic Solvent-Mediated Co-Crystallization. *Adv. Funct. Mater.* **34**, 2409982 (2024).
38. Zhan, X. et al. 3D laser displays based on circularly polarized lasing from cholesteric liquid crystal arrays. *Adv. Mater.* **33**, 2104418 (2021).
39. Kelly, S. M., Jess, T. J. & Price, N. C. How to study proteins by circular dichroism. *Biochim. Biophys. Acta, Proteins Proteom.* **1751**, 119 (2005).


## Acknowledgements

D.K.Hwang acknowledges financial support from the Korea Institute of Science and Technology (KIST) Institution Program (Grant Nos. 2E33542 and 2V10330-24-P039), KU-KIST School project, and the National Research Foundation of Korea (NRF) (Grant Nos. RS-2023-NR077025 and RS-2024-00461204). J. Ahn acknowledges financial support from the Junior Faculty Research Support Grant at Changwon National University in 2024, Global - Learning & Academic research institution for Master's·PhD students, and Postdocs (LAMP) Program of the National Research Foundation of Korea (NRF) grant funded by the Ministry of Education (RS-2024-00444460).

## Author contributions

J-J.L., J.A., and D.K.H. initiated this study. J-J.L., S-J.H., J.W.K., J.A. designed the experiments and fabricated the devices. J-J.L., C.S., S.H., Jihy.K., Jo.K., Y.K., and S-k.A. designed and fabricated the polarimetric kernel arrays. J.P.H., J.J., Jiho.K., B-S.Y., J.A.L., G.W., and S-k.A. contributed in terms of the materials and analysis tools used. C.C. conducted emulation of the chiral decomposition of mixed MNIST patterns and pattern recognition. J-J.L. conducted emulation for mixed-multimodal imaging. J-J.L. and D.K.H. wrote the draft of the manuscript, and all authors contributed to the scientific interpretations as well as the editing of the manuscript.

## Competing interests

The authors declare no competing interests.

## Additional information

**Supplementary information** The online version contains supplementary material available at https://doi.org/10.1038/s41467-025-59935-4.

**Correspondence** and requests for materials should be addressed to Suk-kyun Ahn, Jongtae Ahn or Do Kyung Hwang.

**Peer review information** *Nature Communications* thanks Jiayue Han, Lang Jiang and Mingjie Li for their contribution to the peer review of this work. A peer review file is available.